

Reactivity and Stability of Co-Ni/Al₂O₃ Oxygen Carrier in Multicycle CLC

Mohammad M. Hossain and Hugo I. de Lasa

Dept. of Chemical and Biochemical Engineering, Chemical Reactor Engineering Center, The University of Western Ontario, London, ON, Canada N6A 5B9

DOI 10.1002/aic.11188

Published online May 9, 2007 in Wiley InterScience (www.interscience.wiley.com).

This study deals with the development of a bimetallic Co-Ni/Al₂O₃ oxygen carrier suitable for a fluidized bed chemical-looping combustion process. Temperature programmed characterization shows that the addition of Co enhances the reducibility of the oxygen carrier by influencing the metal-support interactions helping the formation of reducible nickel species. Reactive characterization of the prepared oxygen carriers in a CREC fluidized riser simulator, using multiple reduction/oxidation cycles, demonstrates that the Co-Ni/Al₂O₃ particles display excellent reactivity and stability. The addition of Co in the bimetallic Co-Ni/Al₂O₃ influences the state of the surface minimizing the formation of nickel aluminate. The addition of Co also inhibits metal particle agglomeration by maintaining consistent metal dispersion during the cyclic oxidation/reduction processes. A solid-state kinetics for both reduction and oxidation cycles is established using a clarified Avrami-Erofeev model at nonisothermal conditions. This random nucleation model describes solid phase changes adequately. The activation energy for Co-Ni/Al₂O₃ reduction is found to be significantly lower than the activation energy for the unpromoted Ni/Al₂O₃ sample, with this observation confirming the positive influence of adding Co on the Ni-Al₂O₃ oxygen carrier. © 2007 American Institute of Chemical Engineers AIChE J, 53: 1817–1829, 2007

Keywords: CO₂ capture, CLC, bimetallic oxygen carrier, reactivity, stability

Introduction

Since the beginning of the twentieth century, it has been acknowledged that the emission of greenhouse gases (e.g. CO₂, CH₄, and NO_x) is the main contributor to global warming, with CO₂ being the most prevalent of these emissions. Statistics indicate that the CO₂ concentration in the atmosphere has increased to 368 ppm from a preindustrial value of 280 ppm. As a result the world climate is changing rapidly.¹

The combustion of fossil fuels is considered to be a major source of CO₂. Power generation using fossil fuels contributes one-third to the total CO₂ released,² with the released CO₂ being a function of the type of fuel combusted. Among

the fossil fuels, natural gas produces the lowest CO₂ levels. In this respect, it has been shown that combustion of natural gas can reduce CO₂ emissions by 50% as compared to coal.³

In 1997, the Kyoto Protocol was ratified setting the stage for an international effort to reduce CO₂ emissions. To achieve this goal, a number of CO₂ sequestration technologies are currently being developed. Processes based on chemical absorption and heat induced CO₂ capture or physical adsorption and pressure induced CO₂ recovery, are rather costly and display low energy efficiency. As a result, important research is currently being developed to improve efficiencies and to reduce CO₂ sequestration cost.⁴

Chemical-looping combustion (CLC) is possibly the most promising of the CO₂ sequestration technologies. CLC was originally proposed as a way of increasing thermal efficiency in power plants. More recently, it was identified as having inherent advantages for CO₂ capture.^{5,6} CLC involves two

Correspondence concerning this article should be addressed to H. I. de Lasa at hdelasa@eng.uwo.ca.

interconnected fluidized beds, a fuel reactor and an air reactor, with a solid oxygen carrier recirculated between the two units (Figure 1). In the fuel reactor, the gaseous fuel is combusted using the structural oxygen of the metal oxide. CLC is a flameless combustion taking place at 700–800°C with negligible NO_x formation. The reduced oxygen carrier is then transported to the air reactor to be reoxidized. Completed this operation, the oxygen carrier is recirculated back to the fuel reactor. In CLC, complete combustion of the fuel produces CO_2 and water vapor. Therefore, CO_2 can be recovered easily by condensing the water vapor, without involving an energy intensive CO_2 extra separation step. Finally, the free-of-water CO_2 can be sequestered or/and used for other applications. Regarding the outlet gas stream of the air reactor, it contains nitrogen and unreacted oxygen. These gases can be directly released to the atmosphere with minimum environmental effects.

Concerning CLC, its large-scale application is contingent to the availability of suitable oxygen carriers. Transition metal oxides, such as nickel, copper, cobalt, iron and manganese, are good oxygen carrier candidates. The aforementioned metal oxides are adequate for CLC, given their favorable reductive/oxidative thermodynamic properties. Apart from thermodynamics, oxygen carrier particles should have high oxidation and reduction activity, stability under repeated oxidation/reduction, mechanical strength in fluidized beds, and resilience to agglomeration.^{1,2,7,8} Other important considerations for a successful oxygen carrier are its costs and its environmental impact.

To increase reactivity, durability, and fluidizability, oxygen carrier particles are prepared by depositing the active metal oxide phase on an inert support, such as SiO_2 , TiO_2 , ZrO_2 , Al_2O_3 , and YSZ (Hossain MM, de Lasa HI. Development of novel chemical-looping combustion (CLC) for inherent CO_2 separation—a review. *Int J Chem React Eng* 2007, submitted). While iron and copper based oxygen carriers are comparatively cheaper, the nickel-based materials display important advantages. Nickel can withstand higher temperatures, a favorable factor for high gas turbines performance.⁹ Another important feature of nickel is given by its very low volatility below 1100°C.¹⁰

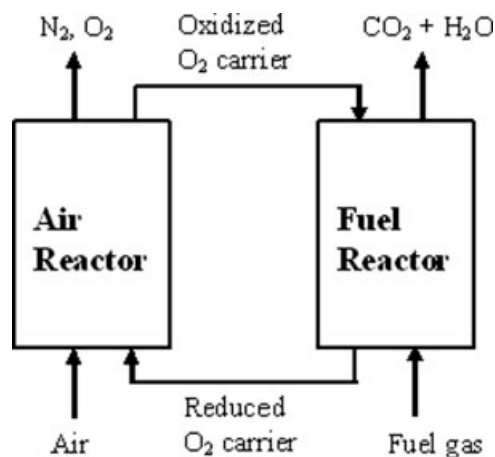


Figure 1. Chemical-looping combustion process.

Since originally recommended by Sinfelt,¹¹ bimetallic (or multimetallic) catalysts were found valuable for hydrocarbon reforming and other petrochemical processes. A similar concept can be considered for CLC bimetallic oxygen carriers with higher reactivity and regenerability under repeated reduction and oxidation. Incorporation of a second metal may prevent phase transformation and/or coke formation. Recently, Adanez et al.¹² reported a stable bimetallic Cu-Ni/ Al_2O_3 oxygen carrier. It was claimed that Cu and Ni stabilized each other displaying improved performance at higher reaction temperature and high oxygen carrying capacity.

Jin et al.¹³ were the first researchers to explore the feasibility of a bimetallic CoO-NiO/YSZ oxygen carrier material for CLC. This oxygen carrier was prepared with equimolar NiO and CoO amounts showing excellent regenerability under repeated reduction/oxidation cycles. In this respect, XRD results showed that NiCoO_2 formation is responsible for oxygen carrier stability. In spite of this, the Co-Ni/YSZ did not receive further consideration due to its poor thermal stability.

Regarding nickel-cobalt bimetallic carriers they can be supported on thermally stable fluidizable Al_2O_3 . Co having important affinity to interact with Al_2O_3 forms cobalt aluminate. Thus replacing a relatively small fraction of nickel by an equivalent amount of cobalt appears to help minimizing the undesirable formation of nickel aluminate.¹⁴

From the earlier discussion, this contribution considers fluidizable bimetallic Co-Ni/ Al_2O_3 oxygen carriers for CLC. These oxygen carriers with 10–40 Ni/Co ratios are prepared and characterized using thermochemical analysis. The high performance of the bimetallic oxygen carrier is established in a fluidized bed CREC riser simulator. It is shown that small amounts of Co provide improved reactivity and stability to nickel under cyclic reduction and oxidation.

Experimental

Preparation of the oxygen carrier

The bimetallic oxygen carriers of the present study were prepared via an incipient wetness technique. With this end, 70 μm $\alpha\text{-Al}_2\text{O}_3$ (65 wt % Al_2O_3 , 34.8 wt % H_2O , 0.15 wt % Na_2O) particles with 20 m^2/g specific surface area from Stream Chemicals were used as the support. Three steps were involved in oxygen carrier preparation: support impregnation, reduction, and calcination. In the impregnation step, aliquots of nitrate solution [$\text{Co}(\text{NO}_3)_2 \cdot 6\text{H}_2\text{O}$ and $\text{Ni}(\text{NO}_3)_2 \cdot 6\text{H}_2\text{O}$] were introduced into the vacuum-sealed Al_2O_3 under continuous mixing conditions. The resultant paste was dried slowly in a furnace by increasing the temperature from ambient to 140°C over 6 h. The dried sample was then transferred to a specially designed fluidized bed reactor located in an oven contacting it with a flowing reducing gas mixture (10% hydrogen molar fraction basis and balanced helium). During oxygen carrier reduction phase, the bed temperature was raised from ambient to 750°C over 4 h and maintained at 750°C for 8 h. This thermal treatment decomposes nitrates [$\text{Co}(\text{NO}_3)_2$ and $\text{Ni}(\text{NO}_3)_2$] into oxides (CoO and NiO), reducing them further into their metallic form. Impregnation, calcinations, and reduction steps were repeated until the desired metal loading was reached. Once the desired metal loading was attained, the oxygen carrier was calcined in air and the

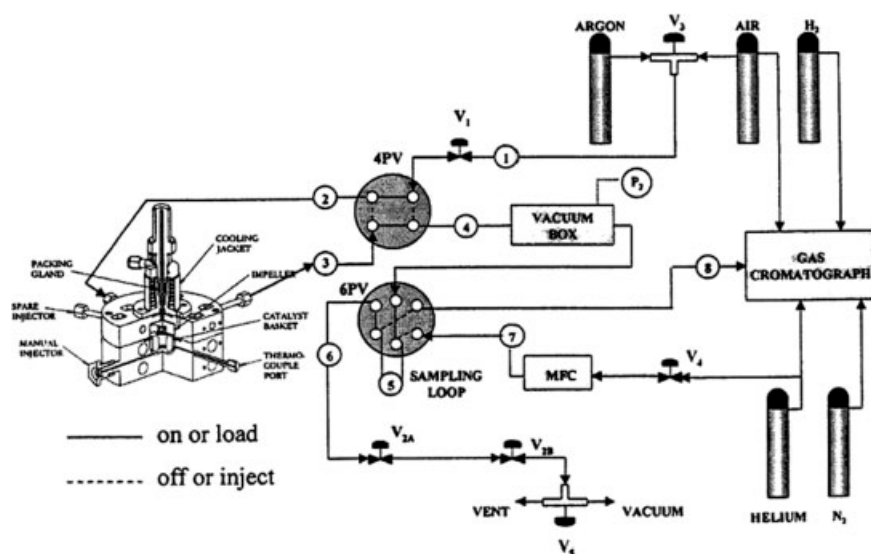


Figure 2. CREC riser simulator (quarter section view) experimental setup.

oven temperature was raised from ambient to 750°C using the same temperature ramp as used for reduction.

TPR/TPO and pulse chemisorption characterization

Temperature programmed reduction (TPR), temperature programmed oxidation (TPO), and pulse chemisorption were conducted in this study using a Micromeritics AutoChem II 2920 analyzer. A 100–200 mg of oxygen carrier sample was loaded in a U-shaped quartz reactor tube and this tube was placed into the sample port, located inside a heating element. The specifics of analysis are described in upcoming subsections.

TPR/TPO

To perform the TPR test, a stream of gas containing 10% H₂ and 90% Ar was circulated through a bed of the prepared oxygen carrier particles at a rate of 50 mL/min. Temperature was raised from ambient to 750°C at a rate of 10°C/min. A thermal conductivity detector (TCD) was used to analyze the gas leaving the bed. Hydrogen reacted with the oxide(s) with increasing the temperature. The TCD data was further processed to calculate the amount of hydrogen consumed during the reduction process.

TPO was developed following each one of the TPR experiments. The procedure for TPO characterization began by flowing a stream of 5% O₂ and 95% He gas through a bed of oxygen carrier particles (now in its reduced form) at a rate of 50 mL/min. The bed temperature was increased from ambient to 750°C at a rate of 10°C/min and the TCD analyzed the gas in the exit stream.

Pulse chemisorptions

Pulse chemisorption experiments were conducted to determine active surface area, percent metal dispersion, and active particle size. To perform a pulse chemisorption characterization, a stream of argon gas flowed through a bed of pre-reduced carrier at a rate of 50 mL/min. A series of hydrogen

pulses (1.0 mL) were injected into the system at ambient temperature. A TCD detector analyzed the exit gas from the sample. As hydrogen gas was adsorbed by the sample, peaks were created in the TCD reading of the outlet stream. The pulse chemisorption was completed when two consecutive peaks had the same area.

Reactive characterization in the CREC riser simulator

The reactivity and the regenerability of the prepared oxygen carriers was established using the CREC riser simulator under expected conditions (turbulent fluidized bed and temperature ranges between 600°C and 900°C) of an industrial scale fluidized CLC unit. The CREC riser simulator is a bench scale mini-fluidized bed reactor, invented at CREC-UWO.¹⁵ This mini-fluidized reactor (volume of 50 cm³) was designed for catalyst evaluation and kinetic studies under fluidized bed (riser/downer) reactor conditions. The CREC riser simulator consists of two sections: the upper shell and the lower shell. These shells allow easy access to the reactor to load and unload the oxygen carrier. An impeller, located in the upper section, and a basket containing the solid oxygen carrier, located in the central section, are the main components of the reactor. Upon rotation of the impeller at high speed (up to 7000 rpm), gas is forced both outward in the impeller section and downwards in the outer reactor annulus, causing the solids catalyst to become fully fluidized. A schematic diagram of the CREC riser simulator, along with the gas injector and anemometer location, is illustrated in Figure 2.

For each reaction experiment in the CREC riser simulator, the required amount (maximum 1 g) of solid oxygen carrier was first loaded into the reactor basket and then the reactor was closed. A temperature program was run to heat the system to the desired temperature for the combustion (carrier reduction) reaction. An argon flow was maintained during the heating period to ensure that the reactor system was free from oxygen (air). Once the reactor reached the desired pre-set temperature, the argon flow was arrested and the pressure

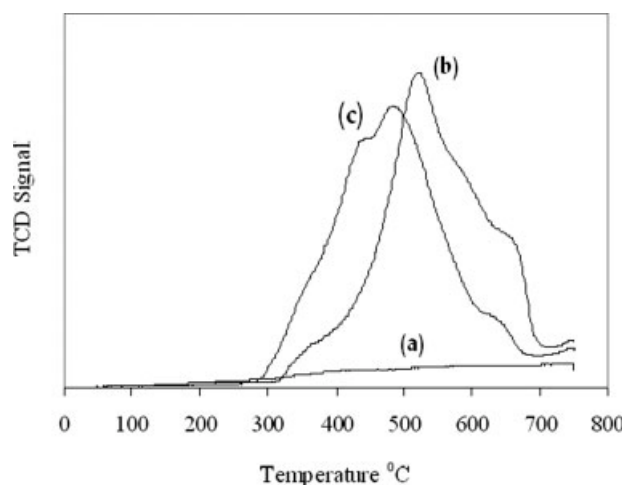


Figure 3. TPR profiles of (a) Co/Al₂O₃, (b) Ni/Al₂O₃, and (c) Co-Ni/Al₂O₃ samples (heating rate: 10°C/min; reducing agent: 10 mol % H₂, balanced Ar at 50 cm³/min)

in the vacuum box was brought to 20.7 kPa (3.0 psi) using a vacuum pump. At this stage the impeller was turned on and the feed (CH₄) was injected into the reactor using a pre-loaded syringe. During this period of methane combustion, the pressure profile of the reactor was recorded using a pressure transducer. At the end of the prespecified reaction time, a valve isolating the reactor and the vacuum bottle was opened and the contents of the reactor were transferred to the vacuum bottle. This introduced an abrupt decrease of the reactor pressure confirming that most of the reactant/product species were removed from the reactor almost instantaneously and that no further reaction took place. Finally, the product species were analyzed using a gas chromatograph. Before the next cycle, the oxygen carrier was regenerated (oxidized) by flowing air at a specified temperature and during a preset reaction time.

Results and Discussion

Temperature programmed studies

In CLC, the solid oxygen carrier undergoes repeated reduction–oxidation cycles. Therefore, a most important characteristic of an oxygen carrier is its reactivity and stability under cyclic operation. To investigate these matters successive TPR and TPO experiments were developed in the context of the present study.

Figure 3 reports TPR spectra of the prepared oxygen carrier samples with the temperature being ramped from 30°C up to 750°C. A TPR profile for Co/Al₂O₃ is also included as a reference. For the Co/Al₂O₃ no clear TPR peak was observed with the hydrogen consumed being relatively small and assigned to the CoO/Co₃O₄ reduction. This modest hydrogen consumption was attributed to the strong cobalt and alumina species interaction. This finding was also supported by a bright blue colored powder obtained once oxygen carrier preparation completed, indicating CoAl₂O₄ formation. Bolt et al.¹⁴ postulated that the counterdiffusion of Co²⁺ and Al³⁺ is responsible for the formation of CoAl₂O₄ species

during the impregnation-drying-reduction processes. The water produced during the reduction stage is also considered to be a main factor for poor reducibility given it promotes enhanced Co-aluminate interactions.¹⁶ Cobalt aluminate, as reported by Mattisson et al.,¹⁷ reduces at comparatively higher temperatures only ($T > 800^{\circ}\text{C}$) and it can therefore be assumed that cobalt aluminate remains unreduced in the temperature range studied.

Regarding the Ni/Al₂O₃ (refer to Figure 3) a single asymmetric TPR peak was observed from 325°C to 700°C. This broad peak displays a maximum at 515°C with its tail being an indication that metal species reduction takes place at higher than 515°C temperatures. There is also a hump at 680°C. This TPR suggest that more than one species contribute to the overall Ni/Al₂O₃ reduction. According to Richardson et al.,^{18–19} NiO and NiAl₂O₄ are reducible phases in the 325–700°C range, with the 680°C hump assigned to nickel aluminate reduction.

Moreover, concerning the bimetallic Co-Ni/Al₂O₃ oxygen carrier its reduction gave similar TPR profiles to the ones for the Ni/Al₂O₃. However, the TPR for Co-Ni/Al₂O₃ has now two humps, one at each side of the maximum TPR peak. The first peak is assigned to the reduction of the dominant metal phases, mainly NiCo₂O₄ and NiO. In this respect, Hardiman et al.^{20–22} also found, the aforementioned species, in a similar catalyst material for steam reforming of methane/ethane. While Hardiman et al.^{20–22} attributed the lower temperature hump to Co₃O₄/NiCo₂O₄/NiO and the higher to NiAl₂O₄, it is doubtful that in our study (refer to the blank runs) that the Co₃O₄ phase contributes to the TPR peak at lower temperatures. One can also notice that the combined areas of the right and left side hump for the bimetallic Co-Ni/Al₂O₃ sample are (~15%) larger than the ones for the Ni/Al₂O₃, with this supporting a higher reducibility of the bimetallic oxygen carrier phases. Another important observation for the bimetallic TPR peak is the 45°C shift toward lower temperatures, a clear indication of the higher reactivity of the bimetallic oxides.

Figure 4 reports TPO peaks for both Ni/Al₂O₃ and CoNi/Al₂O₃. One can observe a comparatively sharper TPO peak for the bimetallic oxygen carriers with a right hand shoulder shifted towards lower temperatures. The shifting of both the reduction and oxidation peaks towards lower temperatures also indicates that the formation of difficult to reduce aluminate phases is minimized with the formation of easily reducible phases (NiO) being enhanced. Therefore, it could be concluded that the addition of Co induces two important effects: (a) limited formation of metal species on the supported Ni/Al₂O₃, (b) larger abundance of very reactive nickel species.

The promotion effects of Co can be explained by applying the site-preference energy concept. The site preference concept is based on the assumption that metal cations in its oxidized state (Ni²⁺ or Co²⁺) with lower bonding energies are the favored to interact with Al₂O₄^{2–}. Thus, Co with a bonding energy of 13 kJ/mol is likely to compete more effectively for the Al₂O₃ sites than Ni, with 50 kJ/mol bonding energy.¹⁴ Thus, in a bimetallic CoNi/Al₂O₃ sample the addition of Co enhances the CoAl₂O₄ abundance minimizing the NiAl₂O₄.

The presence of NiO species on the cobalt doped oxygen carrier was qualitatively confirmed given the dominant sample green color. This green color was in sharp contrast with

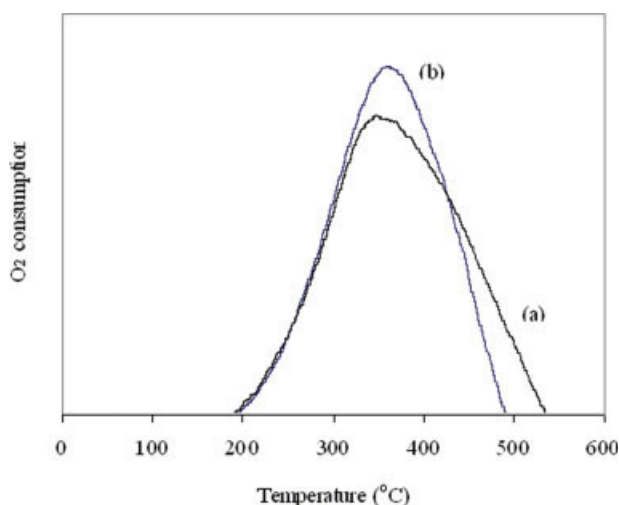


Figure 4. TPO profiles of (a) Ni/Al₂O₃ and (b) Co-Ni/Al₂O₃ samples (heating rate: 10°C/min; reducing agent: 5 mol % oxygen, balanced He at 50 cm³/min).

[Color figure can be viewed in the online issue, which is available at www.interscience.wiley.com.]

the bluish color of the Ni on Al₂O₃, which suggests that an important Ni fraction is in the NiAl₂O₄ form.

In agreement with these findings, Takanabe et al.²³ claimed that the improved titania supported Co-Ni reducibility can be assigned to an homogeneous Co-Ni alloy, while Hardiman et al.^{21,22} considered that the enhanced reducibility of the oxygen carriers is due to the formation of NiO and NiCo₂O₄ mixtures.

Furthermore, the effects of Ni/Co change on the bimetallic Co-Ni/Al₂O₃ carrier material were analyzed in this study using cyclic TPR-TPO experiments. Metal dispersion and redispersion of the reduced carrier was determined by pulse chemisorption (H₂) following each TPR measurement. Figure 5 displays the reducibility and metal dispersion for the bimetallic Co-Ni/Al₂O₃ oxygen carriers at different Ni/Co loadings. Results show that both the percent reduction of loaded metal and metal dispersion decreased with increasing Ni/Co ratio with crystallites achieving stable properties for Ni/Co >30. Thus, for Ni/Co <30, the nickel crystal growth is possibly the main factor for the sharp decrease of reducibility. Phase transformation (NiO/Al₂O₃ ↔ NiAl₂O₄) and/or metal sintering are other possible causes for the loss of active Ni phase.^{24,25} Thus, cobalt doped in the proper amounts can lead to very effective and stable oxygen carriers minimizing the formation of nonreducible species and crystallite growth.

CREC riser simulator studies

The reactivity and stability of the bimetallic Co-Ni/Al₂O₃ oxygen carrier was analyzed in the CREC fluidized riser simulator using methane and air for the combustion and regeneration cycles respectively. The combustion reaction was carried out at 650°C and atmospheric pressure while the carrier reoxidation was conducted at 525°C and atmospheric pressure. The length of the fuel combustion cycles was varied

between 20 and 60 s. Complete reoxidation of the reduced oxygen carrier was achieved in airflow for 10 min.

Generally a high temperature (900–1000°C) is preferable for the down stream turbine operations of a power generation process. However, these conditions may lead to formation of NO_x in the oxidizer reactor and one of the main claimed advantages of CLC, to eliminate NO_x formation, may not be realized. A high reaction temperature also causes metal sintering and particle agglomeration, both phenomena having strong detrimental effects on the supported oxygen carriers activity.⁹ Thus, there is lot of technical potential and implementation value to consider the CLC in a lower temperature range, as in the present study, restricting the evaluation of the oxygen carriers to temperatures below 750°C (the highest temperature level used for TPR/TPO experiments).

Using the experiments developed in the CREC riser simulator, one can notice, that the reduction for both the unpromoted and the Co promoted oxygen carriers is similar, with methane reacting rapidly to form CO₂ and H₂O. The upper curve of Figure 6 displays a typical pressure profile during methane combustion in the CREC riser simulator, showing an increase in total pressure from injection to termination due to an increase in the number of moles upon reaction between methane and the solid oxygen carrier. The lower curve represents the pressure profile of the vacuum box, which remained constant during the reaction. At termination point the reactor pressure is abruptly decreased to vacuum box pressure and vacuum box pressure is slightly increased showing complete transfer of gas from reactor to the vacuum box. Concerning the interpretation of fuel combustion results one can consider the following reactions:

Combustion cycle:

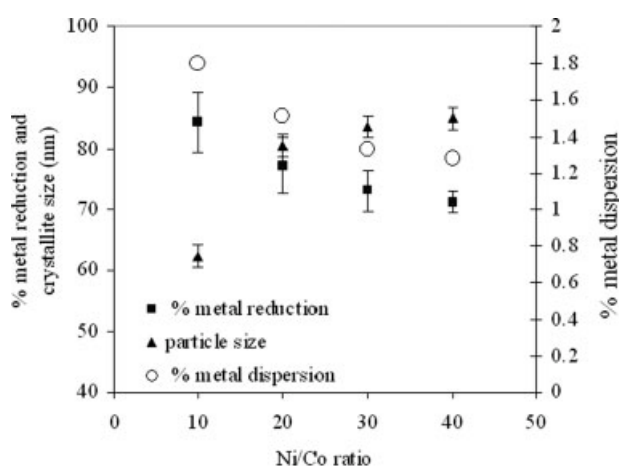
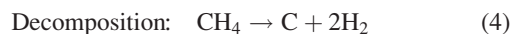
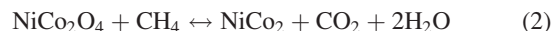
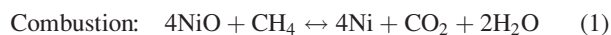


Figure 5. Effects of the variation of Ni/Co ratios on the reducibility, dispersion and crystal size of the bimetallic Co-Ni/Al₂O₃ oxygen carrier.

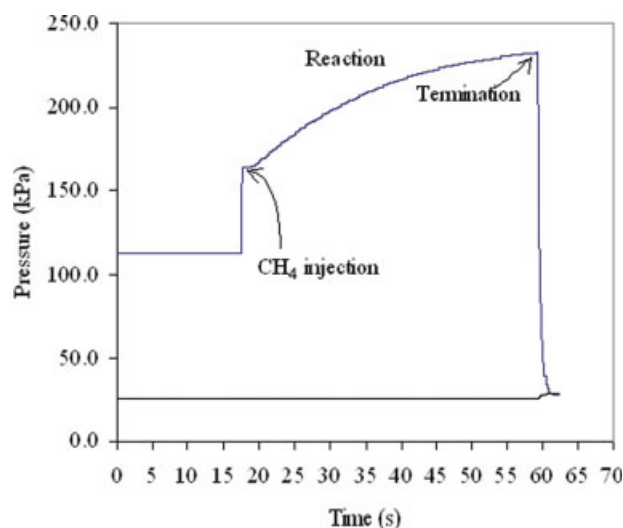
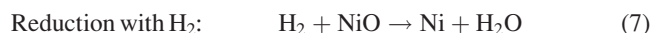
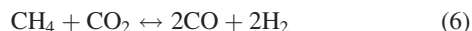
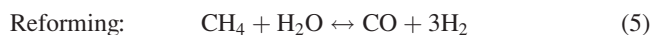


Figure 6. Pressure profile in the CREC riser simulator for methane combustion with oxide particles.

[Color figure can be viewed in the online issue, which is available at www.interscience.wiley.com.]

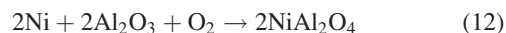


Analysis of the gases from the CREC riser simulator showed both CO_2 and H_2O . The product analysis also showed trace amounts of hydrogen; with no CO being detected in the combustion product gas sample. From this observation, it is assumed that the combustion of methane with the nickel based oxygen carriers (both unpromoted and Co promoted) proceeds according to reactions 1–3. The presence of trace amounts of H_2 in the product gas indicates the occurrence of some methane decomposition and reforming. Furthermore, H_2 formation via methane decomposition was confirmed by product analysis during the oxygen carrier regeneration cycle (discussion to follow).

Product selectivity during methane combustion with a supported metal oxide is mainly associated with the degree of the reduction of the oxygen carrier.^{10,12} At the beginning of the reaction (or short contact time), the fully oxidized oxygen carrier favors the total oxidation of methane to form CO_2 and H_2O . As the reaction proceeds, the partially reduced oxygen carrier catalyzes the reforming reactions producing synthesis gas (CO , H_2O). It is equally important to point out that both CO and H_2 are very reactive with the metal oxide under the studied reaction conditions being quickly converted to CO_2 and H_2O , respectively. Therefore, it can be assumed that the CO and H_2 produced via reforming reactions are further oxidized forming CO_2 and H_2O (reactions 7 and 8). Consequently, no CO was detected as a product of methane combustion while using the oxygen carriers of the present study.

On the other hand, oxygen carrier regeneration can be described with the following set of reactions:

Regeneration cycle:



Resistance to coke formation is a property of paramount importance for oxygen carrier performance. Deposited carbon leads to CO or/and CO_2 formation in the regeneration cycle (reaction 13). One has thus, to minimize carbon formation to attain high CO_2 capture efficiencies. In the present study, the outlet gas analysis from the carrier re-oxidation cycle (regeneration) showed negligible amounts of CO and/or CO_2 , with this being an indicator of little carbon formed during reduction cycle and of the high performance of the oxygen carrier under consideration.

Regarding carbon formation, it is acknowledged that reaction times during the fuel combustion cycle may play a crucial role.¹² In this respect, reaction times selected for reaction testing in the CREC riser simulator were restricted to 10–60 s and this to prevent methane decomposition (reaction 4).

Methane and nickel oxide conversions were two important parameters assessed in the present study, with these two parameters defined as follows:

(a) Methane conversion was calculated from the product analysis data using Eq. 14, since CO_2 is the only carbon-bearing component in the methane combustion product,

$$X_{\text{CH}_4} = \frac{C_{\text{CO}_2, \text{out}}}{C_{\text{CH}_4, \text{out}} + C_{\text{CO}_2, \text{out}}} \times 100\% \quad (14)$$

(b) Nickel oxide(s) conversion was determined on the basis of the number of moles of reacted oxygen, the weight of the carrier and the nickel composition of the carrier.

Figure 7 displays the methane and oxygen carrier conversion during the combustion cycle for various reaction times. As it can be noticed in Figure 7, a maximum 80% methane conversion was observed with the bimetallic sample, with the highest methane conversion remaining in the 70% for the unpromoted carrier. Therefore, a significant improvement of methane conversion was observed using the bimetallic carrier. The blank runs were developed for confirmation that both combustion and re-oxidation (650°C and 525°C, respectively) were adequate, with these blank runs showing a very low conversion in all cases (Figure 7).

In CLC fuel conversion cycle, it is highly desirable that complete combustion of methane be achieved.^{12,26} The higher operating temperature is also favorable given higher reactor temperatures lead to a higher inlet temperature to the downstream gas turbine and as a result increased efficiency. However, the high reaction temperature also accelerates the

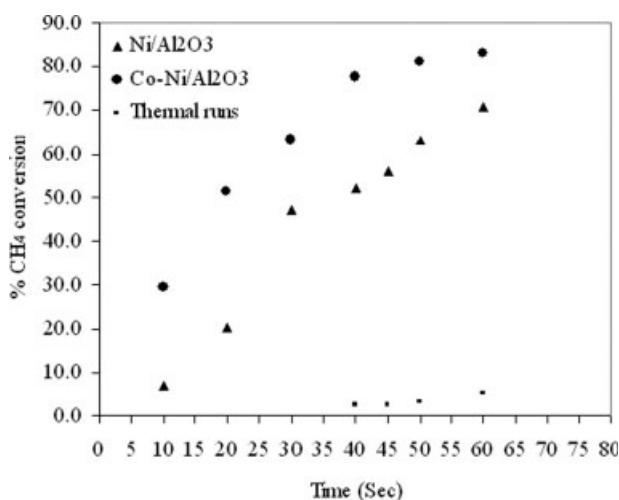


Figure 7. Conversion of methane and oxygen carriers in CREC fluidized bed riser simulator (T : 650°C ; P : 1 atm; W_{carrier} : 40 mg; V_{CH_4} inj.: 10 ml).

formation of nickel aluminate, which is difficult to reduce/oxidize. To avoid metal sintering, some researchers recommend the use of two fluidized bed reactors for fuel combustion instead of one to maintain a relatively low operating temperature. In this process configuration, the outlet gas from the first fluidized bed reactor enter the second fluidized bed reactor where the unreacted methane is combusted completely with fresh oxygen carrier.¹² This two fluidized bed concept could likely be considered for bimetallic oxygen carriers such as the one of the present study.

Considering that oxygen carrier reactivity follows closely the methane conversion parameter one can conclude reviewing Figure 7 that the reduction of Co-Ni/Al₂O₃ takes place more readily than the Ni/Al₂O₃ reduction. The Co-Ni/Al₂O₃ reaches its highest level of conversion at 45 s while, the Co-Ni/Al₂O₃ displays comparable conversions at longer reaction times. Thus, consistent with the TPR results, the addition of Co aids the formation of easily reducible nickel oxides minimizing nickel-support interaction and formation of nonreactive nickel aluminate.

Following the encouraging reactivity results and to be able to assess oxygen carrier stability, the bimetallic Co-Ni/Al₂O₃ carrier was evaluated over multiple CLC cycles. Figure 8 reports methane conversion results as a function of the number of reduction/oxidation cycles. It is proven with these results that the bimetallic Ni(5)/Al₂O₃ displayed a stable conversion during repeated CLC cycles. The addition of Co can also favorably modify metal-support interactions, as assessed via the energies of hydrogen desorption.²⁷

Figure 9 reports XRD of a fresh sample and a regenerated sample after 10 CLC cycles. XRD diffraction patterns show that the crystalline phase of the bimetallic oxygen carrier remains unchanged over TPR/TPO cycles. These results are in agreement with the findings of Jin et al.¹³ using Co-Ni/YSZ (yttria-stabilized zirconia) in a CLC processes. Thus, XRD shows that the bimetallic carrier microstructure, obtained from solid solution of Co and Ni, leads to stable oxygen carrier of high performance.

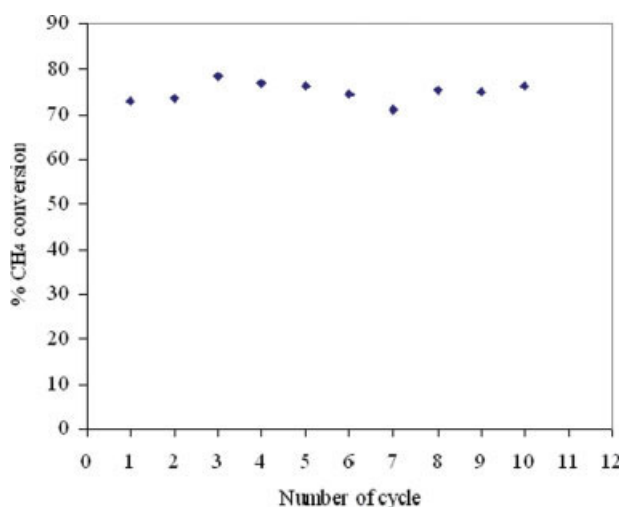


Figure 8. Conversion of methane in multiple CLC cycles in CREC fluidized bed riser simulator (T : 650°C ; P : 1 atm; W_{carrier} : 40 mg; V_{CH_4} inj.: 10 ml).

[Color figure can be viewed in the online issue, which is available at www.interscience.wiley.com.]

Kinetics modeling of temperature programmed data

The reduction and/or oxidation of oxygen carriers is a multistep process. Like other heterogeneous reactions, the overall reaction rate of solids involves diffusion, adsorption and intrinsic reaction steps. Depending on the nature of the reducible species, one of the above steps or their combination can control the overall reaction.

TPR and TPO experiments were carried out, in this study, in a packed bed of 70 μm particles. Experiments were carried out such that the reaction system could be modeled as a differential reactor.

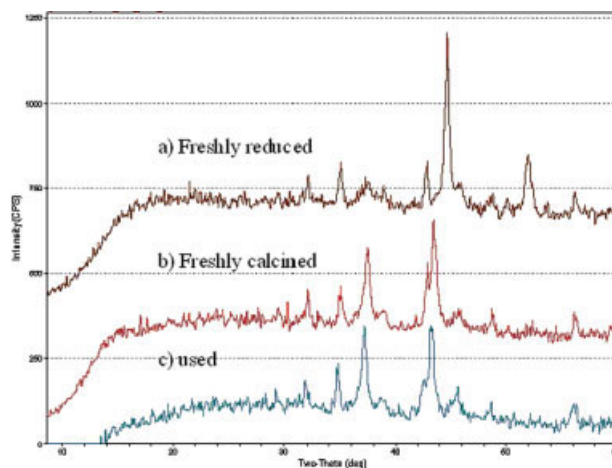


Figure 9. X-ray diffractograms of (a) freshly reduced (b) freshly calcined and (c) used (10 CLC cycles) Co-Ni/Al₂O₃ samples.

[Color figure can be viewed in the online issue, which is available at www.interscience.wiley.com.]

Table 1. Parameters Used to Evaluate Mass Transfer Limitations

| Parameter | Gas Phase Reactants | | Remarks |
|---------------------------------------|----------------------|------------------------|--|
| | H ₂ | O ₂ | |
| D_{eff} (cm ² /s) | 7.3×10^{-1} | 1.054×10^{-1} | Estimated as 0.1 D_{AB} , where D_{AB} was the molecular diffusion, which was calculated by using Fuller's correlation ²⁹ |
| C_{A} (mol/L) | 4.1×10^{-3} | 2.05×10^{-3} | Concentration of the gas phase reactant was calculated using ideal gas law for 10% H ₂ and 5% O ₂ gas mixtures |
| $-r'_{\text{A}}$ (mol/g solid/s) | 2.4×10^{-6} | 1.0×10^{-6} | Calculated for highest conversion level (at peak) |
| R_{p} (cm) | 1×10^{-2} | 1×10^{-2} | Considering largest size of particle as 100 μm . |
| ρ_{p} (g/cc) | 8×10^{-1} | 8×10^{-1} | The density change of the oxygen carrier particle due to reaction was negligible |

The external transport limitation of the differential reactor can be assessed from the Sherwood number with Froessling's dimensionless correlations.²⁸

$$Sh = 2 + 1.1Sc^{0.33}Re^{0.6} \quad (15)$$

$$k_{(\text{c})} = \frac{ShD_{(\text{AB})}}{d_{\text{p}}} \quad (16)$$

$$(C_{\text{Ag}} - C_{\text{As}})_{\text{film}} = \Delta C_{\text{film}} = \frac{(-r'_{\text{A(obs)}})}{k_{\text{c}}} \quad (17)$$

Where, Sh , Sc , and Re are Sharwood, Schmidt, and Reynolds numbers, respectively. k_{c} is the external mass transfer coefficient (cm/s), D_{AB} molecular diffusivity (cm²/s), d_{p} is the particle diameter (cm), $-r'_{\text{A(obs)}}$ is the observed reaction rate (mol/g solid. s), C_{Ag} is the bulk concentration of gaseous reactant, and C_{As} is the surface concentration of gaseous reactant (mol/L). Equation 17 was evaluated at worst possible conditions, i.e., the lowest value of Sh equals 2, which occurs at stagnant fluid conditions around the solid particle. This lowest value corresponds to the possible highest gas film resistances (minimum value of mass transfer coefficient). The calculated values of ΔC_{film} (Eq. 17) are 0.00002 and 0.00005 mmol/m³ for reduction and oxidation cycles respectively. The negligible concentration variation of the gas phase reactant in the bulk phase and the oxygen carrier surface indicates negligible effects of the external mass transfer limitations.

Regarding intraparticle diffusion, its influence was assessed using the Weisz-Prater criterion.²⁸ Internal mass transfer is considered negligible if the following inequality is satisfied:

$$C_{\text{WP}} = \frac{-r'_{\text{A(obs)}}\rho_{\text{p}}R_{\text{p}}^2}{D_{\text{eff}}C_{\text{AS}}} < 1 \quad (18)$$

where, $-r'_{\text{A(obs)}}$ is the observed reaction rate (mol/g solid. s), ρ_{p} is the particle density (g/cc), R_{p} is the particle radius (cm), D_{eff} is the effective diffusivity (cm²/s), and C_{AS} is the concentration of gaseous reactant at the surface of solid particles (mol/L).

To evaluate Eq. 18, it is often practical bounding the potential influence of intraparticle mass transfer using a worst-case scenario situation, i.e. the upper limit for estimated reaction rates. Thus, $-r'_{\text{A(obs)}}$ was considered as follows: (a) maximum hydrogen/oxygen consumption rate during the TPR/TPO analysis, (b) D_{eff} evaluated with minimum

expected diffusion coefficient, (c) C_{AS} set at minimum hydrogen/oxygen concentrations in the gas phase. Calculated C_{WP} values are 0.000064 and 0.00037 for reduction and oxidation respectively and this confirms the negligible influence of intraparticle diffusion. Various parameters required for the evaluation of Eq. 17 and Eq. 18 is reported in Table 1.

Thus, the intrinsic TPR/TPO kinetics can be formulated considering an overall reaction rate being a function of the degree of reduction of solid material $f(\alpha)$ and the composition of the species in the gas-phase^{30,31}:

$$\frac{d\alpha(t)}{dt} = k(T)f(\alpha)f(p_{\text{H}_2/\text{O}_2}, p_{\text{H}_2\text{O}}) \quad (19)$$

where α is the progress of the reaction, which can be expressed in different ways based on the available measured variable(s). Usually, the extent of reaction is defined in terms of the change of mass of the sample or an equivalent basis in terms of gas consumed, gas evolved, heats consumed, or heat evolved.

In the present study, the degree of reduction and oxidation of the supported oxygen carriers is defined using the hydrogen and oxygen consumption data, for the respective reactions. On the basis of the TPR/TPO profile analysis, the transient solid conversion (α) during each solid-state reaction can be obtained from:

$$\alpha(t) = \frac{\Delta n_t}{\Delta n_{\text{total}}} \quad (20)$$

where Δn_t represents the moles of hydrogen or moles of oxygen consumed at time t (min) and Δn_{total} the total moles of hydrogen or moles of oxygen consumed for the complete reduction or oxidation of the oxygen carrier sample.

The function $f(p_{\text{H}_2/\text{O}_2}, p_{\text{H}_2\text{O}})$ of Eq. 19 can be lumped in a single pseudoconstant given all the TPR experiments were carried out at same feed flow rate, hydrogen/oxygen partial pressure, hydrogen essentially free of water, and differential conversion. Under these assumptions Eq. 19 can be reduced to,

$$\frac{d\alpha(t)}{dt} = k(T)f(\alpha) \quad (21)$$

with the rate constant (k) given by the Arrhenius equation

$$k = k_0 \exp \left[\frac{-E_{\text{app}}}{R} \left(\frac{1}{T} - \frac{1}{T_{\text{m}}} \right) \right] \quad (22)$$

Table 2. Avrami-Erofeev Models

| Value of n | Mechanism | Model Formulation |
|--------------|---|--|
| n | Avrami-Erofeev model | $f(\alpha) = n(1 - \alpha)[- \ln(1 - \alpha)]^{(n-1)/n}$ |
| 1 | Random nucleation | $f(\alpha) = 1 - \alpha$ |
| 2 | 2-dimensional nuclei growth (2D Avrami-Erofeev model) | $f(\alpha) = 2(1 - \alpha)[- \ln(1 - \alpha)]^{1/2}$ |
| 3 | 3-dimensional nuclei growth (3D Avrami-Erofeev model) | $f(\alpha) = 3(1 - \alpha)[- \ln(1 - \alpha)]^{2/3}$ |

where E_{app} is the activation energy and k_0 the pre-exponential factor and T_m being the centering temperature to minimize cross-correlation between parameters. The function of the degree of conversion ($f(\alpha)$) depends on the model applied in the determination of the kinetics. Both empirical and mechanistic models are available in the technical literature.^{30,32} Richardson et al.¹⁹ suggested that the reduction of alumina supported NiO involves the following: (i) dissociation of hydrogen molecule (initially by metal oxide during the induction period, then by previously formed Ni as the reduction front advances into the grain), (ii) surface diffusion of atomic hydrogen to a reduction center, (iii) rupture of metal oxide bond, (iv) nucleation of the metal atom into metallic cluster, and (v) growth of metal cluster into metal crystallites. Any one or combination of the earlier steps may control the reduction rate.

Other possible issues of reduction of supported carriers via TPR/TPO are the accessibility of the metal oxide grains with this being a function of the support material properties. Thus, shape, size, and pore size distribution are all factors affecting reducibility of oxide sites. Regarding metal support-interaction, there is a preferred orientation of the active component, which mainly depends on the chemical nature of the support material.^{18,19} In some cases the support is modified or a modifier/promoter is added to the support to minimize the metal support interactions enhancing the reducibility of the catalyst. According to Shon and Szekely,³³ the reduction of supported nickel oxide is a process controlled by the intrinsic chemical reaction step. Thus, the decreased activation energy directly contributes to the increased reactivity of the promoted oxygen carrier.

Brown³⁴ reviewed alternating models to describe gas-solid kinetics and its effects on the α - t (conversion-time) sigmoid profiles. Following an induction period, both reduction and oxidation involve multiple steps, such as formation of nuclei, crystal growth, dislocation, and point defects.

This type of conversion function ($f(\alpha)$) may be described in terms of the reaction-rate controlling Avrami-Erofeev (A-E) model^{18,20,35,36}. This model was originally applied to describe the kinetics of phase transformations of steel. Latter on, it found numerous applications in kinetics of crystallization, precipitation, decomposition of various solids, thin film growth, and polymerization. Recently, this model has been successfully used to analyze the TPR and TPO reduction and oxidation data of both bulk and supported metal oxides.^{19,20,30,31,34}

According to the Avrami-Erofeev model, the reduction and oxidation of the supported metal oxide proceeds through nucleation and a possible crystal growth with this leading as described in the Appendix to the following equation,

$$f(\alpha) = n(1 - \alpha)[- \ln(1 - \alpha)]^{\frac{(n-1)}{n}} \quad (23)$$

where n is the Avrami exponent indicative of the reaction mechanism and crystal growth dimension. Different values of the n parameter lead, as reported in Table 2, to various random nucleation, 2-dimensional nuclei growth and 3-dimensional nuclei growth.

Substituting Eqs. 22 and 23 into Eq. 21 and after rearrangement the following form of equation is obtained:

$$\frac{d\alpha(t)}{dt} = nk_0 \exp\left[\frac{-E_{\text{app}}}{R}\left(\frac{1}{T_o + \beta t} - \frac{1}{T_m}\right)\right] (1 - \alpha)[- \ln(1 - \alpha)]^{\frac{(n-1)}{n}} \quad (24)$$

with T_0 being the initial temperature and β the heating rate.

A least square fitting of the k_0 , E_{app} , and n parameters of Eq. 24 was implemented using MATLAB and experimental data of this study. The evaluation of three model parameters was developed using 120 data points (taken once every 2 s) under conditions where the oxygen carrier sample was heated from room temperature to 730°C at 10 °C/min. Thus, the degree of freedom for model evaluation in this ample range of temperatures was $120 - 3 = 117$. Parameters were estimated in 0–0.95 conversion range. Given the R^2 values and spans of the parameters obtained, it was concluded that the Avrami-Erofeev model better fitting of was achieved using an n value of one. For instance for $n = 2$ the R^2 values were 0.8 instead of 0.99 and the spans were increased from 5–10% to 20–30%.

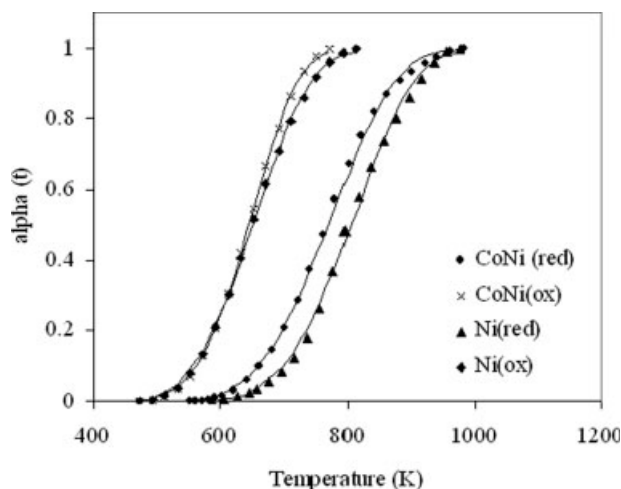


Figure 10. Conversion $[\alpha(t)]$ plots for non-isothermal reduction/oxidation of (a) Ni/Al₂O₃ and (b) Co-Ni/Al₂O₃ samples (the solid lines are the model predicted values).

Note: Reported points are one every 2 min to avoid the figure to be overcrowded. The original data file includes data points taken every 2 s.

Table 3. Estimated Parameters for TPR and TPO Cycles Using Avrami-Erofeev Model with $n = 1$

| Sample ID | *Red./Ox. | E (kJ/mol) | k_0 | R^2 | † Cor. |
|--------------------------------------|-----------|--------------|------------------------------|-------|-----------------|
| Ni/Al ₂ O ₃ | Red. | 53.5 ± 2 | $(269 \pm 5) \times 10^{-4}$ | 0.99 | 0.54 |
| Co-Ni/Al ₂ O ₃ | Red. | 45.1 ± 1 | $(260 \pm 4) \times 10^{-4}$ | 0.99 | 0.51 |
| Ni/Al ₂ O ₃ | Ox. | 45 ± 2 | $(376 \pm 4) \times 10^{-4}$ | 0.99 | 0.95 |
| Co-Ni/Al ₂ O ₃ | Ox. | 44 ± 2 | $(324 \pm 3) \times 10^{-4}$ | 0.99 | 0.97 |

*Red./Ox., Reduction/Oxidation.

 † Cor., Correlation coefficient.

However, a “ n ” value of 1 or random nucleation model was selected given the close to constant crystallite size hypothesized, during repeated reduction and oxidation cycles (Figure 5), which is an indication of the very limited crystallite growth between cycles. Figure 10 shows the comparison between the experimental and model (for $n = 1$) predicted conversions during reduction and oxidation cycles of the oxygen carrier samples. To avoid Figure 10 to be overcrowded, only the experimental data points taken every 2 min are reported (also refer to the footnote in the figure caption). One can notice that when data points are compared with model predictions there is a normal distribution of residuals with high correlation coefficients.

Table 3 reports the estimated parameter values with 95% confidence intervals and correlation coefficients (R^2). The model parameters were calculated with reduced spans ($\pm 5\%$), which indicates excellent fitting of the experimental data and confirms the adequacy of the Avrami-Erofeev model. The estimated values of activation energy are 53.5 ± 2 kJ/mol, with this value being consistent with values reported in the literature.³² As shown in the Appendix of this manuscript the apparent kinetic constant (k) is a function of both nucleation and crystal growth processes, with estimated energy of activation being a difference between activation energy for nucleation and activation energy for particle growth.

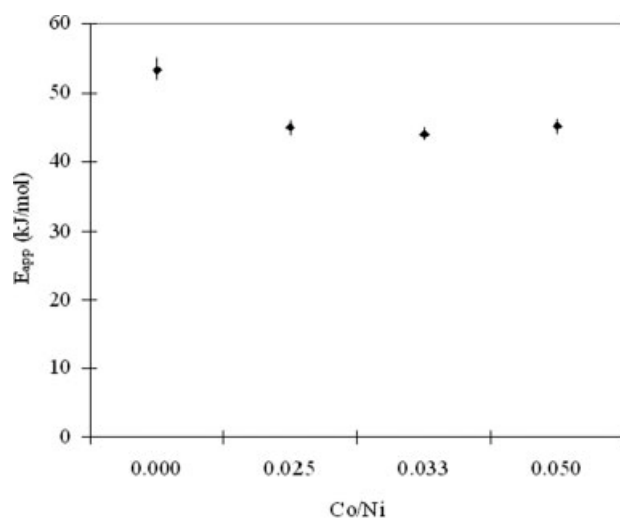
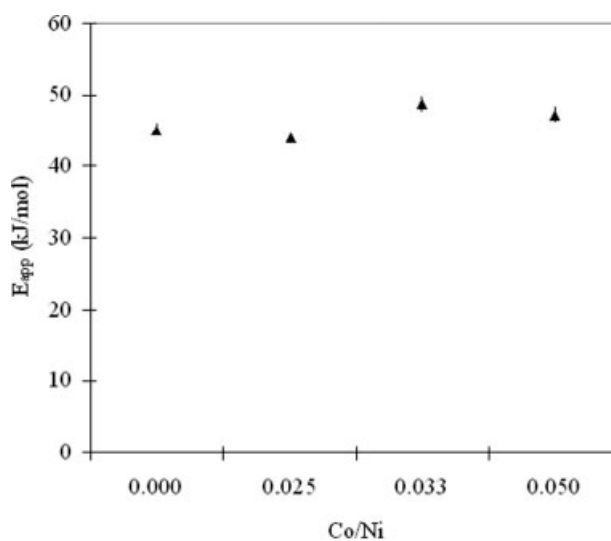
Regarding the activation energy for the Co promoted sample, one can notice that it falls to 45.1 ± 1 kJ/mol, an energy of activation considerably lower than the one for the unpromoted sample.

As discussed earlier, the nickel aluminate interacts more readily with the alumina support, involving a 53.5 ± 2 kJ/mol energy of activation. Therefore, the unpromoted sample requires higher activation energy with this reflecting the increased difficulty of reducing the nickel phase in the oxygen carrier.

Figure 11 displays the estimated activation energies of the bimetallic Co-Ni/Al₂O₃ oxygen carriers at different Ni/Co loadings. After an initial decrease, the activation energy remained almost unchanged with an increasing Ni/Co ratio. This observation suggests that small amounts of Co are adequate to modify the Ni-alumina interactions.

As already stated, activation energies for both Ni-alumina unpromoted carrier and Ni-alumina Co promoted carrier reduction may be described as a difference between activation energy for nucleation and crystal growth (refer to Eq. A21 of the Appendix). As a result, changes of measured activation energy may simply reflect nucleation and crystal growth energy of activation relative variations and one should be cautious with the phenomenological interpretation of these changes.

Concerning activation energies for oxidation, both the Ni/Al₂O₃ and Co-Ni/Al₂O₃ samples showed similar values within 95% confidence limits with this being true for all levels of doped cobalt considered (Figure 12). These results show that the state of the oxygen carrier either Ni/Al₂O₃ and/or Co-Ni/Al₂O₃ has negligible effect on the kinetics of the oxidation reaction. These findings can be explained considering that once the reduction is completed, nickel is present

**Figure 11. Activation energy for reduction of Co-Ni/Al₂O₃ sample at different Co/Ni ratios.****Figure 12. Activation energy for oxidation of Co-Ni/Al₂O₃ sample at different Co/Ni ratios.**

as Ni^0 species in all cases. Therefore, it is reasonable to observe that both materials display close reactivity and energies activation during the oxidation cycle.

Conclusions

The following are the conclusions of the present study:

- TPR/TPO studies showed that the addition of Co enhances the reducibility of the oxygen carrier by influencing the metal-support interaction forming easily reducible nickel species.
- Pulse chemisorption demonstrates that appropriate Ni/Co ratios can provide better metal dispersion/redispersion. It is hypothesized that doped cobalt interacts more readily with the alumina support, inhibiting the nickel aluminate formation.
- Reactive characterization in a fluidized bed CREC riser simulator shows that during multiple reduction/oxidation cycles with CH_4 and air, the Co-Ni/ Al_2O_3 display excellent reactivity and stability.
- XRD of Co doped oxygen carrier, both fresh and used, display similar XRD diffraction patterns confirming minimum agglomeration of the nickel species over high temperature oxidation/reduction processes.
- The Avrami-Erofeev model with random nucleation mechanism with $n = 1$ is found to describe the experimental data adequately, with various parameters being determined with their appropriate statistical spans for good fitting.
- The activation energies for Co-Ni/ Al_2O_3 reduction is found to be in the 45 kJ/mol level significantly lower than the 54 kJ/mol activation energies for the unprompted Ni/ Al_2O_3 reduction, with this confirming the favorable effect of Co on the reducibility of the bimetallic oxygen carrier.

Acknowledgments

M.M.H. gratefully acknowledges the National Sciences and Engineering Research Council of Canada (NSERC) for Canada Graduate Scholarship for Doctoral study (CGS-D) and The University of Western Ontario for President's Scholarship for Graduate Study (PSGS). The authors thank NSERC for their financial support to this project.

Notation

| | |
|-----------------------|---|
| C_{AS} | = concentration of hydrogen at the surface of solid particles (mol/L) |
| C_{CH_4} | = mole composition of CH_4 in the combustion product |
| P_{CO_2} | = mole composition of CO_2 in the combustion product |
| D_{eff} | = effective diffusivity, cm^2/s |
| E_{app} | = apparent activation energy for oxidation/reduction (kJ/mol) |
| E_{nuc} | = activation energy for nucleation (kJ/mol) |
| E_{grow} | = activation energy for particle growth, kJ/mol |
| K_s | = shape factor of the growing particles |
| k | = specific rate of the overall reaction, moles/sec |
| k_{nuc} | = specific rate of nucleation, number of nuclei/sec |
| k_{grow} | = specific rate constant for nuclei growth |
| N | = number of growing nuclei |
| N_0 | = number of potential nucleation sites |
| n | = dimensions of the growing crystals |
| R_p | = particle radius, cm |
| $-r'_{\text{A(obs)}}$ | = observed reaction rate, mol/g solid. s |
| T | = temperature, K |

| | |
|-------------------------|---|
| T_m | = centering temperature, (K) |
| t | = time, s |
| u | = Heaviside function |
| V_{total} | = volume of the reacted solid oxygen carrier, cm^3 |
| V_0 | = volume of the reducible species, cm^3 |
| X_{CH_4} | = conversion of methane |
| α | = degree of conversion of oxygen carrier |
| α_{total} | = extended degree of conversion of the oxygen carrier |
| β | = rate of temperature increase (K/min) |
| η | = constant |
| ρ_p | = particle density g/cc |
| τ | = activation time of the nuclei, s |

Literature Cited

- Cho P, Mattisson T, Lyngfelt A. Comparison of iron-, nickel-, copper-, and manganese-based oxygen carriers for chemical-looping combustion. *Fuel* 2004;83:1245–1225.
- Lyngfelt A, Leckner B, Mattisson T. A fluidized-bed combustion process with inherent CO_2 separation; application of chemical-looping combustion. *Chem Eng Sci*. 2001;56:3101–3113.
- Naqvi R, Bolland O, Brandvoll O, Helle K. Chemical looping combustion-analysis of natural gas fired power cycles with inherent CO_2 capture. In Proceedings of ASME Turbo Expo, 2004, Power for land, sea and air, June 14–17, Vienna, Austria.
- Halmann M, Steinberg M. Greenhouse Gas Carbon Dioxide Mitigation: Science And Technology. Boca Raton, FL: Lewis Publishers, 2000.
- Richter HJ, Knoche KF. Reversibility of combustion processes. *ACS Symp Ser*. 1983;235:71–85.
- Ishida M, Jin H. CO_2 recovery in a power plant with chemical looping combustion. *Energy Convers Manag*. 1997;38:187–192.
- Mattisson T, Johansson M, Lyngfelt A. Multicycle reduction and oxidation of different types of iron oxide particles-application to chemical-looping combustion. *Energ Fuel*. 2004;18:628–637.
- Adanez J, de Diego LF, Garcia-Labiano F, Gayan P, Abad A. Selection of oxygen carriers for chemical-looping combustion. *Energ Fuel*. 2004;18:371–377.
- Wolf J, Anheden M, Yan J. Comparison of nickel- and iron-based oxygen carriers in chemical looping combustion for CO_2 capture in power generation. *Fuel* 2005;84:993–1006.
- Villa R, Cristiani C, Groppi G, Lietti L, Forzatti P, Cornaro U, Rosini S. Ni based mixed oxide materials for CH_4 oxidation under redox cycle conditions. *J Mol Catal A: Chem*. 2003;204/205:637–646.
- Sinfelt JH. *Bimetallic Catalysts: Discoveries, Concepts and Applications, An Exxon Monograph*. Wiley: New York, 1983.
- Adanez J, Garcia-Labiano F, de Diego LE, Gayan P, Celaya J, Abad A. Nickel-copper oxygen carriers to reach zero CO and H_2 emissions in chemical-looping combustion. *Indus Eng Chem Res*. 2006;45:2617–2625.
- Jin H, Okamoto T, Ishida M. Development of a novel chemical-looping combustion: synthesis of a looping material with a double oxide of CoO-NiO. *Energ Fuel*. 1998;12:1272–1277.
- Bolt PH, Habraken FHPM, Geus JW. Formation of nickel, cobalt, copper, and iron aluminates from α - and γ -alumina-supported oxides: a comparative study. *J Solid State Chem*. 1998;135:59–69.
- de Lasa HI. Riser Simulator for Catalytic Cracking Studies, US Patent 5,102,628, 1992.
- Storsaeter S, Totdal B, Walmsley JC, Tanem BS, Holmen A. Characterization of alumina-, silica-, and titania-supported cobalt Fischer-Tropsch catalysts. *J Catal*. 2005;236:139–152.
- Mattisson T, Johansson M, Lyngfelt A. Reactivity of some metal oxides supported on alumina with alternating and oxygen-application of chemical-looping combustion. *Energ Fuel*. 2003;17:643–651.
- Richardson JT, Turk B, Twigg MV. Reduction of model steam reforming catalysts: effect of oxide additives. *Appl Catal A: General*. 1996;148:97–112.
- Richardson JT, Scates RM, Twigg MV. X-ray diffraction of hydrogen reduction of NiO/ α - Al_2O_3 steam reforming catalysts, *Appl Catal A: General*. 2004;267:35–46.
- Hardiman KM, Hsu CH, Ying TT, Adesina AA. The influence of impregnating pH on the postnatal and steam reforming characteristics of a Co-Ni/ Al_2O_3 catalyst. *J Mol Catal A: Chem*. 2005;239:41–48.

21. Hardiman KM, Cooper CG, Adesina AA. Multiple analysis of the role of preparation conditions on the intrinsic properties of Co-Ni/Al₂O₃ steam-reforming catalyst. *Ind Eng Chem Res.* 2004;43:6006–6013.
22. Hardiman KM, Ying TT, Adesina AA, Kennedy EM, Dlugogorski BZ. Performance of a Co-Ni catalyst for propane reforming under low steam-to-carbon ratios. *Chem Eng J.* 2004;102:119–130.
23. Takanabe K, Ngaoka K, Nariai K, Aika K. Titani-supported cobalt and nickel bimetallic catalysts for carbon dioxide reforming of methane. *J Catal.* 2005;232:268–275.
24. Ishida M, Jin H. A novel gas turbine cycle with hydrogen-fueled chemical-looping combustion. *Int J Hydrogen Energy.* 2000;25:1209–1215.
25. Ding RG, Yan ZF. Structure characterization of the Co and Ni catalysts for carbon dioxide reforming of methane. *Catal Today.* 2001;68:135–143.
26. Mattisson T, Johansson M, Lyngfelt A. The use of NiO as an oxygen carrier in chemical looping combustion. *Fuel* 2006;85:736–747.
27. Hossain MM, Sedor KE, de Lasa HI, Co-Ni/Al₂O₃ oxygen carrier for fluidized bed chemical-looping combustion: desorption kinetics and metal support interaction. *Chem Eng Sci.* 2007; doi: 10.1016/j.ces. 2006.12.066.
28. Fogler HS. *Element of Chemical Reaction Engineering*, 3rd edition. NJ: Prentice Hall, 1999:758–759.
29. Welty JR, Wicks CE, Wilson RE, Rorrer G. *Fundamentals of Momentum, Heat and Mass Transfer*, 4th edition. New York: Wiley, 2001:435.
30. Kanervo JM, Krause AOI. Kinetics analysis of temperature-programmed reduction: behavior of a CrO_x/Al₂O₃ catalyst. *J Phys Chem B.* 2001;105:9778–9784.
31. Kanervo JM, Krause AOI. Characterization of supported chromium oxide catalysts by kinetics analysis of H₂-TPR data. *J Catal.* 2002; 207:57–65.
32. Richardson JT, Scates RM, Twigg MV. X-ray diffraction study of nickel oxide reduction by hydrogen. *Appl Catal A: General.* 2003; 246:137–150.
33. Sohn HY, Szekeley J. A structural model for gas-solid reaction with moving boundary-III: a general dimensionless representation of the irreversible reaction between a porous solid and a reactant gas. *Chem Eng Sci.* 1972;27:763–778.
34. Brown ME. *Introduction to Thermal Analysis: Techniques and Applications*, 2nd edition. Dordrecht, The Netherlands: Kluwer Academic Publishers, 2001:181–210.
35. Malecka B, Crozdz-Ciesla E, Malecki A. Non-isothermal studies on mechanism and kinetics of thermal decomposition of cobalt (II) oxalate hydrate. *J Therm Anal Calorim.* 2002;68:819–831.
36. Malecka B, Crozdz-Ciesla E, Malecki A. Mechanism and kinetics of thermal decomposition of zinc oxalate. *Thermochem Acta.* 2004;423: 13–18.
37. Avrami M. Kinetics of phase change. I. *J Chem Phys.* 1939;7:1103–1112.
38. Avrami M. Kinetics of phase change. II. *J Chem Phys.* 1940;8:212–224.
39. Avrami M. Kinetics of phase change. III. *J Chem Phys.* 1941;9:177–184.
40. Brown WE, Dollimore D, Galwey AK. Reaction in the solid state. In: Bamford CH, Tipper CFH. *Comprehensive Reaction Kinetics*, Part 22. Amsterdam: Elsevier Scientific, 1980:49–59.

Appendix: Clarifications of Avrami-Erofeev's Model

Avrami-Erofeev's model is based on the combination of nucleation, growth, and impingement of randomly distributed nuclei.^{37–39} The formulation of the general dynamic equation for the interface advance reaction begins with the definition of the total reacted volume of the solid material (V_{total}) as postulated by Karervo and Krause³⁰ and given by the following equation:

$$V_{\text{total}}(t) = \int_0^t V(t, \tau) \left(\frac{dN}{dt} \right)_{t=\tau} d\tau \quad (\text{A1})$$

Where $\left(\frac{dN}{dt} \right)_{t=\tau}$ represents nucleation rates defined at time $t = \tau$,

N the number of growing nuclei and

$V(t, \tau)$ is the volume of nucleus at time t , which became activated at time τ .

To solve Eq. A1 important assumptions have to be adopted vis-à-vis of the crystal nucleation (crystal agglomeration) rate. A first assumption can consider that the rate of nucleation is related to the difference between N_0 , the potential nucleus formation sites and the number of growing nuclei, N as follows:

$$\left(\frac{dN}{dt} \right) = k_{\text{nuc}}(N_0 - N) \text{ or as an alternate } \left(\frac{dN}{dt} \right)_{t=\tau} = k_{\text{nuc}} N_0 e^{(-k_{\text{nuc}} \tau)} \quad (\text{A2})$$

Thus, the rate of nucleation involves the N_0 , a function of nickel loading and k_{nuc} and τ , two parameters significantly affected by the specific support selected for the oxygen carrier.

Furthermore for n -dimensional particle growth the volume of the nucleus at time t can be expressed as:

$$V(t, \tau) = K_s [k_{\text{grow}}(t - \tau)u(t - \tau)]^n \quad (\text{A3})$$

Where K_s is the shape factor

k_{grow} is the rate constant for nuclei growth and

n is the number of the linear dimensions in which the nucleus is growing

$u(t - \tau)$ a Heaviside function

Substituting Eqs. A2 and A3 into Eq. A1 yields

$$V_{\text{total}}(t) = \int_0^t K_s [k_{\text{grow}}(t - \tau)u(t - \tau)]^n k_{\text{nuc}} N_0 e^{-k_{\text{nuc}} \tau} d\tau \quad (\text{A4})$$

Since the nuclei is considered to appear at time τ , the lower limit of the integral in Eq. A4 can be replaced by τ , with $u(t - \tau) = 1$ at $t > \tau$. Thus,

$$V_{\text{total}}(t) = \int_{\tau}^t K_s [k_{\text{grow}}(t - \tau)]^n k_{\text{nuc}} N_0 e^{-k_{\text{nuc}} \tau} d\tau \quad (\text{A5})$$

The analytical solution of Eq. A5 following successive integration by parts can be expressed as,

$$V_{\text{total}}(t) = \frac{K_s N_0 k_{\text{grow}}^n n!}{k_{\text{nuc}}^n} e^{-k_{\text{nuc}} \tau} (-1)^{n+1} \times \left[e^{-k_{\text{nuc}}(t-\tau)} - \sum_{i=0}^n (-1)^i \frac{(t-\tau)^i}{i!} \right] \quad (\text{A6})$$

Dividing both sides of Eq. A6 by V_0 , the initial reducible or oxidizable species volume, one can expressed the total volume using a dimensionless α_{total} parameter as follows:

$$\alpha_{\text{total}}(t) = \frac{K_s N_0 k_{\text{grow}}^n n!}{V_0 k_{\text{nuc}}^n} e^{-k_{\text{nuc}} \tau} (-1)^{n+1} \times \left[e^{-k_{\text{nuc}}(t-\tau)} - \sum_{i=0}^n (-1)^i \frac{(t-\tau)^i}{i!} \right] \quad (\text{A7})$$

However, given that the growing nuclei may reach the boundaries of the other growing particles or ingest germ nuclei, Avrami³⁷ and Erofeev⁴⁰ considered two functions: α representing the number of reacted sites and its complement $(1-\alpha)$ representing the sites still available for either oxidation or reaction. According to this, $d\alpha$ is related to the fractional change $d\alpha_{\text{total}}$ as $(1-\alpha)^{38,40}$. Thus,

$$\frac{d\alpha/dt}{d\alpha_{\text{total}}/dt} = 1 - \alpha \quad (\text{A8})$$

This linear relationship (Eq. A8) has been further verified in the case of the present study by calculating $\frac{d\alpha_{\text{total}}}{dt}$ from the model predicted values of α and $\frac{d\alpha}{dt}$. The results showed a good agreement with a linear relationship observed as in Eq. A8 (coefficient of regression = 0.95)

Integration and rearrangement of Eq. A8 gives:

$$\alpha_{\text{total}} = -\ln(1 - \alpha) \quad (\text{A9})$$

Substituting Eq. A9 into Eq. A7 gives:

$$-\ln(1 - \alpha) = \frac{K_S N_0 k_{\text{grow}}^n n!}{V_0 k_{\text{nuc}}^n} e^{-k_{\text{nuc}} \tau} (-1)^{n+1} \left[e^{-k_{\text{nuc}}(t-\tau)} - \sum_{i=0}^n (-1)^i \frac{(t-\tau)^i}{i!} \right] \quad (\text{A10})$$

For cases where $t > \tau$, case of the present study, the right hand side of Eq. A10 can be approximated with the highest order term of the series:

$$-\ln(1 - \alpha) = \frac{K_S N_0 k_{\text{grow}}^n}{V_0 k_{\text{nuc}}^n} e^{-k_{\text{nuc}} \tau} t^n \quad (\text{A11})$$

Or alternatively Eq. A11 can be expressed using a constant k lumping group of parameters:

$$-\ln(1 - \alpha) = (kt)^n \quad (\text{A12})$$

$$\alpha = 1 - e^{-(kt)^n} \quad (\text{A13})$$

with, $K^n = \frac{K_S N_0 k_{\text{grow}}^n n!}{V_0 k_{\text{nuc}}^n} e^{-k_{\text{nuc}} \tau}$

Once Eq. (A13) is established the following relations can be obtained:

$$\frac{d\alpha}{dt} = nk^n t^{n-1} e^{-(kt)^n} \quad (\text{A14})$$

$$e^{-(kt)^n} = 1 - \alpha \quad (\text{A15})$$

$$kt = [-\ln(1 - \alpha)]^{1/n} \quad (\text{A16})$$

Therefore on the basis of Eqs. A14, A15, and A16 the change of α with oxidation or reduction time-on-stream can be represented as:

$$\frac{d\alpha}{dt} = kf(\alpha) \quad (\text{A17})$$

With $f(\alpha)$ being the Avrami-Erofeev's equation (A18):

$$f(\alpha) = n(1 - \alpha)[- \ln(1 - \alpha)]^{(n-1)/n} \quad (\text{A18})$$

The k lumped parameter of Eq. A17 involves N_0 , V_0 , k_{nuc} , and k_{grow} parameters of both growth and nucleation. However this constant also includes a $e^{\frac{k_{\text{nuc}} \tau}{n}}$ factor:

$$k = \left[\frac{K_S N_0 e^{-k_{\text{nuc}} \tau}}{V_0} \right]^{1/n} \frac{k_{\text{grow}}}{k_{\text{nuc}}} \quad (\text{A19})$$

Clarification of k definition is of significance if one attempts to relate the k parameter with growth and nucleation phenomenologically based kinetic parameters.

Equation A18 is applicable to the reduction of NiO over alumina oxygen carrier given the following: (a) the rate of site reduction/oxidation can be described as a potential function, (b) $t > \tau$ for essentially all conditions considered in this study.

As well Eq. A19 can be further reduced given that the n parameter was found to be very close to 1 (refer to kinetic modeling section), $k_{\text{nuc}} \tau < 1$ for all conditions considered in this study. Thus,

$$k = \left[\frac{K_S - N_0}{V_0} \right] \frac{k_{\text{grow},0}}{k_{\text{nuc},0}} \quad (\text{A20})$$

One can incorporate the effect of temperature on k , considering that both k_{grow} and k_{nuc} follow Arrhenius' type of equations,

$$k = \left[\frac{K_S - N_0}{V_0} \right] \frac{k_{\text{grow},0}}{k_{\text{nuc},0}} e^{\frac{(E_{\text{grow}} - E_{\text{nuc}})}{RT}} \quad (\text{A21})$$

Thus, Eq. A21 shows that the E_{ap} as defined in section 3.2, can be interpreted as the difference between the activation energy for growth and the activation energy for nucleation.

Manuscript received Dec. 14, 2006, and revision received Mar. 19, 2007.